Thermal radiation in asymmetrically driven coupled non-linear photonic cavities

Bertrand Braeckeveldt* and Bjorn Maes
Micro- and Nanophotonic Materials Group, Research Institute for Materials Science and Engineering, University of Mons, 20 Place du Parc, Mons B-7000, Belgium

(Received 14 February 2023; revised 5 May 2023; accepted 8 May 2023; published 23 May 2023)

We study thermal radiation from a system of two coupled photonic cavities including the nonlinear Kerr effect, using numerical simulations and analytical methods. The general system, which can be implemented as two cavities in a waveguide, is asymmetrically driven with a monochromatic pumping from a single side. We describe the eigenmodes in the linear and nonlinear regime as well as the transmission of the coupled system. These results are then employed to understand the thermal radiation exhibited from both sides as each part of the system is coupled to a bath at a different temperature. Interestingly, the radiation spectrum is complicated, and can present up to four peaks due to the rich nonlinear coupling features. Furthermore, in certain regimes these spectra can drastically change upon variation of the bath temperatures. In addition, interference between the emitted and reflected radiation can lead to dips in the thermal radiation. Moreover, the system can exhibit self-pulsing, leading to comblike spectra for thermal radiation with peaks of very large amplitude. Our proposed analytical model for thermal radiation in the stable regime fits very well with the numerical results and describes a general class of devices.

DOI: 10.1103/PhysRevB.107.174310

I. INTRODUCTION

The study of thermal radiation from microstructures finds current applications in energy devices [1–3] as well as in nanotechnology [4,5] and imaging via thermal microscopy [6–9]. Interest in micro/nanoscale thermal radiation has not stopped expanding since Rytov developed a fluctuation-dissipation approach for thermal electromagnetic fields [10–12]. Using this theory, for example, it has been demonstrated that nanostructured bodies can exhibit thermal radiation in the near-field larger than the blackbody limit [13].

Radiative heat transfer in nonlinear media was also investigated, e.g., leading to thermal broadening due to two-photon absorption and a non-Lorentzian emissivity due to self-phase modulation [14]. In particular, thermal radiation was studied in the case of a single driven Kerr cavity where it can present Stokes and anti-Stokes side peaks, whose relative amplitudes can be tuned by tailoring the temperatures [15]. Recently, dynamic time modulation in photonic systems resulted in a photon-based active cooling mechanism with performance approaching the Carnot limit [16]. This temporal modulation can also instigate stochastic resonance induced by thermal fluctuations, leading to a frequency shift in the coherent response of the system [17].

Driven nonlinear oscillators, such as optical resonators, were widely studied over the past decades [18–20]. When these resonators are coupled, they present many interesting effects, such as symmetry breaking and self-pulsing [21,22], where the response is oscillating with a constant pump. In this paper, we consider these coupled cavities with thermal fluctuations, which will be modeled as noise sources [14,15]. As in previous works [23,24], we assume the Markov approximation, avoiding temporal correlation of the sources. Other works treat the case of systems with memory, e.g., in optical systems with noninstantaneous nonlinearities where it has been employed for energy harvesting [25].

In particular, in this paper, we extend the model of thermal radiation from a single Kerr photonic cavity [15], towards a coupled system made of two cavities, which, in practice, can be coupled, e.g., via an intermediate waveguide connecting both resonators. We investigate the effect of the relative temperatures in the system to modify the shape of the radiation spectra, which are quite complicated, and can be tailored to a large degree. Furthermore, we examine the presence of parametrically unstable regimes and their influence on the emitted radiation, which can present "supernarrow" peaks in certain regimes.

First, in Sec. II, we present the typical geometry and the coupled-mode theory equations. To efficiently depict the results, in Sec. III, we propose a rewriting of these equations by using effective parameters. As thermal fluctuations act as perturbations on the system, we perform an eigenmode analysis in both the linear and nonlinear regimes. Section IV describes the eigenmodes (Sec. IV A) and the transmission function (Sec. IV B) in the linear regime. The same kind of analysis is then performed in the nonlinear regime in Sec, V with a perturbative description (Sec. V A) and a transmission function (Sec. V B). In Sec. VI, we explore thermal radiation spectra in both the linear (Sec. VI A) and the nonlinear (Sec. VI B) regime. Finally, in Sec. VI C, we demonstrate that relative temperatures drastically change these spectra before concluding.

*bertrand.braeckeveldt@umons.ac.be

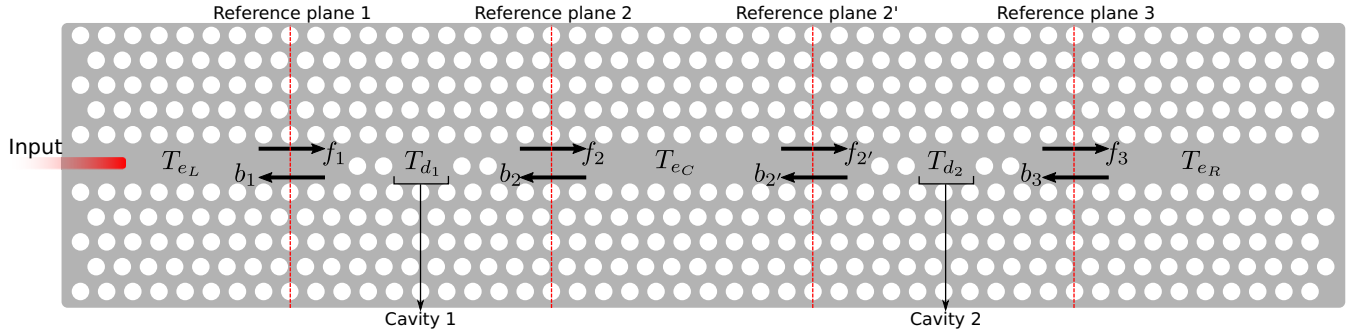

FIG. 1. Photonic crystal geometry with two cavities coupled via a central waveguide. The system is excited with a monochromatic pump via the left waveguide. Temperatures of left, central, and right waveguides as well as cavities 1 and 2, are controlled independently.

II. NUMERICAL MODEL

We consider a geometry consisting of two coupled photonic cavities that are single-mode and present nonlinearities of the Kerr type. Such a system can be implemented in a photonic crystal circuit, e.g., as represented in Fig. 1, but other structures with standard waveguides and rings are feasible as well. We assume that the cavities are sufficiently far from each other, so that the coupling arises only from the central waveguide with no direct coupling. Furthermore, the length of the waveguides is sufficiently small, so we neglect their losses. Even if we neglect losses inside the waveguides, there are dissipation channels for the cavities: The first one is the coupling to the waveguides, and the second one is internal dissipation in the cavities.

As pictured in Fig. 1, the system can be driven from one or both sides, however, in this paper, we focus on single-side asymmetric driving via a monochromatic pump with constant intensity. The cavity mode amplitude evolution is accurately described using coupled-mode theory with the Langevin framework [15,26,27]. Using a rotating frame at the pump frequency (see Appendix A),

$$\frac{d\psi_1}{d\tau} = [-j(\Delta + |\psi_1|^2) - 1]\psi_1 + je^{j\frac{\phi}{2}}(f_1 + \xi_{e_L}) + je^{j(\phi/2)}(b_2 + \xi_{e_C}) + \xi_{d_1} \tag{1}$$

$$b_1 = e^{j\phi}(f_1 + \xi_{e_L}) + j\kappa e^{j(\phi/2)}\psi_1 \tag{2}$$

$$\frac{d\psi_2}{d\tau} = [-j(\Delta + |\psi_2|^2) - 1]\psi_2 + je^{j(\phi/2)}\left(f_2 + \xi_{e_{C'}}\right) + je^{j(\phi/2)}\left(b_3 + \xi_{e_R}\right) + \xi_{d_2} \tag{3}$$

$$f_3 = e^{j\phi}\left(\underbrace{b_3}_{0} + \xi_{e_R}\right) + j\kappa e^{j(\phi/2)}\psi_2 \tag{4}$$

where ψ_i is the dimensionless mode amplitude of the cavity i. The dimensionless forward and backward fields in the waveguide i are, respectively, f_i and b_i. As the pumping is from the left side, $b_3 = 0$ in Eq. (4). The reduced time τ is expressed in terms of the total dissipation rate γ of the cavities ($\tau = \gamma t$). Each cavity is coupled to two ports and can support internal losses. The total decay rate γ in each cavity is the sum of the coupling to left and right channels, respectively, γ_{e_L} and γ_{e_R} as well as internal losses γ_d. The latter corresponds to coupling to phonons or other internal dissipative decay channels in the cavity.

We consider equal coupling to the left and right channels ($\gamma_{e_L} = \gamma_{e_R} = \gamma_e/2$) and the same internal dissipation for both cavities (same γ_d). To summarize, for each cavity, the total dissipation rate is $\gamma = \gamma_e + \gamma_d$. We introduce the relative coupling $\kappa = \gamma_e/\gamma \leqslant 1$, the ratio between external and total dissipation rates. This coupling is the same for both cavities. We consider the same resonant frequency ω_0 for the cavities as well. The detuning between the pump frequency ω_p and the resonant frequency ω_0 of the cavities is captured via the reduced detuning $\Delta = \dfrac{\omega_p - \omega_0}{\gamma}$.

The reference planes, see Fig. 1, are chosen in order to have the forward and backward fields in the central waveguide given by (see Appendix C)

$$f_2 = \kappa \frac{je^{j\phi/2}\psi_1 + e^{3j\phi/2}\psi_2}{1 - e^{2j\phi}} \tag{5}$$

$$b_2 = \kappa \frac{je^{3j\phi/2}\psi_1 + e^{j\phi/2}\psi_2}{1 - e^{2j\phi}}. \tag{6}$$

In these relations, ϕ represents a phase that depends on the waveguide lengths (so the reference planes) and the photonic crystal waveguide barrier reflection properties.

In Eqs. (1)–(4), the temporal evolution of the fields is stochastic because each waveguide and cavity are described as different baths. These baths are determined by their temperatures, which are set independently. Their thermal fluctuations are modeled with complex white-noise sources ξ_i satisfying the following correlation relations [15,28,29]:

$$\langle \xi_i(\omega)\xi_j^*(\omega')\rangle = \frac{\alpha\gamma_e}{\gamma^3}\Theta(\omega, T_i)\delta(\omega - \omega')\delta_{ij}, \tag{7}$$

$$\langle \xi_k(\omega)\xi_l^*(\omega')\rangle = 2\frac{\alpha\gamma_d}{\gamma^3}\Theta(\omega, T_k)\delta(\omega - \omega')\delta_{kl}, \tag{8}$$

$$\langle \xi_m(\omega)\xi_n(\omega')\rangle = \langle \xi_m^*(\omega)\xi_n^*(\omega')\rangle = 0, \tag{9}$$

where $i, j \in \{e_L, e_C, e_{C'}, e_R\}$, $k, l \in \{d_1, d_2\}$, and $m, n \in \{e_L, e_C, e_{C'}, e_R, d_1, d_2\}$. Interestingly, for the central waveguide, which connects the cavities, two noise sources should be considered: One is added to the forward field arriving at reference plane 2′ ($\xi_{e_{C'}}$) of Fig. 1, and the other term corresponds to the backward field at reference plane 2 (ξ_{e_C}). These noise sources are not correlated with each other, but their amplitudes are equal because there is only one temperature

for the central waveguide. Parameter α in Eqs. (7) and (8) characterizes the strength of the nonlinear interaction and depends on an overlap integral of the linear cavity fields [15] (see Appendix A). In this paper, we consider α real corresponding to self-phase modulation [14,15]. It is possible to account for two-photon absorption (TPA) by choosing a complex α with a nonzero imaginary component. Since TPA affects the total absorption rate depending on the power intensity, it must be included in the fluctuation-dissipation theorem when describing the diffusion coefficient of the noise sources [14]. Finally, $\Theta(\omega, T) = \hbar\omega/[\exp(\hbar\omega/k_B T) - 1]$ is the mean energy of a quantum oscillator in thermal equilibrium with the bath at temperature T. Therefore, the noise intensity in each part of the system is tailored via the temperatures.

III. EFFECTIVE COUPLING AND DETUNING

In this section, we propose a more compact version of the equations by introducing effective coupling and detuning. As there is no direct coupling, the cavities are connected via the central waveguide. Therefore, Eqs. (1) and (3) are coupled via Eqs. (5) and (6) and the field amplitude evolution in cavity i ($\in \{1, 2\}$) can be rewritten

$$\frac{d\psi_i}{d\tau} = -[j(\Delta' + |\psi_i|^2) + \Gamma]\psi_i - jJ\psi_{3-i} + je^{j\phi/2} f_1 \delta_{1,i} + N_i, \tag{10}$$

$$N_i = \xi_{d_i} + je^{j\phi/2}(\xi_{e_L} + \xi_{e_C})\delta_{i,1} + je^{j\phi/2}(\xi_{e_R} + \xi_{e_{C'}})\delta_{i,2}, \tag{11}$$

where N_i contains all the noise sources.

Equation (10) also introduces an intercavity coupling $J = \kappa/(2\sin\phi)$ as well as an effective detuning $\Delta' = \Delta + \kappa/(2\tan\phi)$. These two parameters are affected by the phase ϕ and the relative coupling κ, meaning that the interaction between both cavities only depends on the losses and the phase. This intercavity coupling will be maximum when there is no internal dissipation ($\kappa = 1$), and if the phase tends toward 0 or π. In these limit cases, the cavity amplitudes are either opposite ($\psi_1 = -\psi_2$ for $\phi = 0$) or the same ($\psi_1 = \psi_2$ for $\phi = \pi$), and the intercavity coupling goes to infinity for these phase values. The effective detuning Δ' is larger than Δ when $0 < \phi < \pi/2$ and smaller when $\pi/2 < \phi < \pi$.

Finally, Eq. (10) introduces the effective cavity dissipation as $\Gamma = 1 - \kappa/2$. The latter increases when the relative coupling to the waveguides, $\kappa = \gamma_e/(\gamma_e + \gamma_d)$, decreases. In that case, a larger part of the total dissipation rate is related to internal losses.

The phase dependence of the coupling J, effective detuning Δ', and effective dissipation rate Γ is summarized in Fig. 2 with varying κ. As the phase ϕ goes toward 0 or π, constructive interference in the central waveguide leads to an increase of the coupling J [solid curves in Fig. 2(a)]. Decreasing the relative coupling κ increases losses through internal dissipation and, therefore, leads to smaller intercavity coupling J [curves in Fig. 2(a)] and larger effective dissipation rate Γ [horizontal dotted lines in Fig. 2(a)]. In Fig. 2(b), the deviation from the original detuning Δ becomes larger as the phase is approaching 0 or π and changes sign at $\phi = \pi/2$.

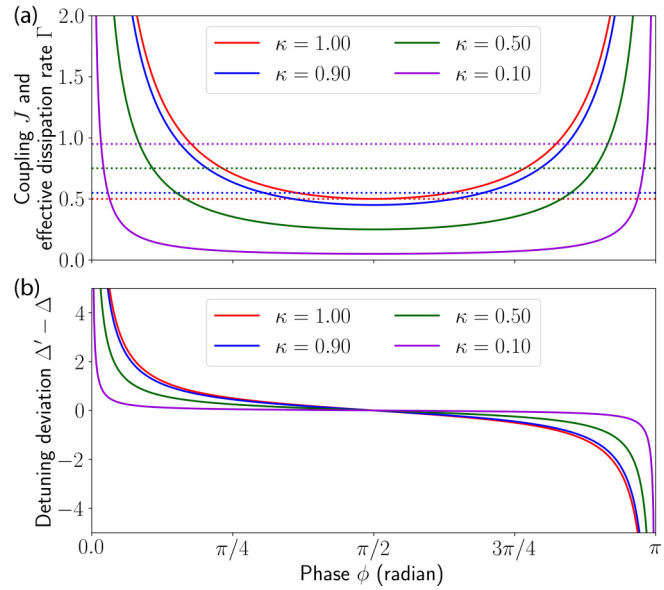

FIG. 2. (a) Intercavity coupling J (curves) and effective dissipation rate Γ (horizontal lines) versus phase ϕ for various relative coupling κ. (b) Change in effective detuning Δ' due to resonant coupling versus phase ϕ for various κ.

IV. LINEAR ANALYSIS

In order to understand the behavior of the coupled system for low input powers, we first perform a linear analysis [$|\psi_i|^2 \simeq 0$ in Eq. (10)]. We examine the eigenmodes as well as the transmission in this particular regime.

A. Eigenmodes

In the absence of pumping $f_1 = 0$ and noise $\xi_i = 0$, the coupled equations of Eq. (10) become

$$\frac{d\Psi}{d\tau} = D_{\text{lin}}\Psi, \tag{12}$$

where $\Psi = (\psi_1, \psi_2)^T$ and D_{lin} is the Jacobian of the linear system. As at equilibrium, we expect a solution of the form $\psi_i \sim e^{\lambda\tau}$, an eigenvalue analysis of D_{lin} leads to

$$\lambda_\pm = -\Gamma - j(\Delta' \mp J). \tag{13}$$

One can show (see Appendix B) that the frequency and damping rate of the two eigenmodes $k \in \{+, -\}$ are

$$\omega_k = \gamma\,\text{Im}(\lambda_k) + \omega_p, \tag{14}$$

$$\gamma_k = \gamma\,\text{Re}(\lambda_k), \tag{15}$$

and that Ψ_+ (Ψ_-) are the eigenvectors of λ_+ (λ_-) correspond to the antisymmetric (symmetric) mode. In our case, with an asymmetric pumping, both modes can be excited [30]. By inspecting Eqs. (13) and (14), one can see that the eigenfrequency of both modes depends on the intercavity coupling J. One can make an analogy with two coupled mechanical oscillators where the eigenmodes depend on the spring constant between both masses. As there are losses in the system, the eigenmodes are damped with a rate equal to the effective dissipation rate Γ.

B. Transmission

The transmission T is defined as the outgoing power from the right waveguide $|f_3|^2$, divided by the pump power $|f_1|^2$ into the left port. By using Eqs. (1)–(6) in the frequency domain, one can show that (see the Supplemental Material [31])

$$T(\omega) = \frac{J^2\kappa^2}{[\Gamma^2 - \Delta'(\omega)^2 + J^2]^2 + 4\Gamma^2\Delta'(\omega)^2}, \tag{16}$$

with $\Delta'(\omega) = \dfrac{\omega - \omega_0}{\gamma} + \dfrac{\kappa}{2\tan\phi}$. The transmission function Eq. (16) possesses three extrema, for

$$\Delta' = \pm\sqrt{J^2 - \Gamma^2} \quad \text{and} \quad \Delta' = 0. \tag{17}$$

As the effective detuning is a real parameter, the first two solutions exist when $J \geqslant \Gamma$. In this situation, these two solutions locate the transmission maxima, wherease $\Delta' = 0$ corresponds to the local minimum. On the other hand, when $J < \Gamma$, there is only one transmission peak located at $\Delta' = 0$. Moreover, it can be shown that when there is no internal dissipation ($\Gamma = 0.5$), a detuning $\Delta = 0$ (pump resonant with cavities) always corresponds to a maximum transmission.

This analysis shows that $J > \Gamma$ gives the condition to observe two transmission peaks. From a physical point of view, the coupling of the two cavities splits the transmission peak of a single cavity into two peaks. The larger the intercavity coupling J, the larger the separation between both peaks. On the other hand, the effective dissipation rate Γ determines the linewidth of the transmission peaks. Therefore, the peaks can only be resolved if the coupling is larger than the effective dissipation rate (linewidth). Thus, for a coupling larger than the effective dissipation rate, two peaks are visible in the transmission spectra (Fig. 3). They reach $\kappa^2/4\Gamma^2$ and are separated by a local minimum transmission of $J^2\kappa^2/(\Gamma^2 + J^2)^2$ for $\Delta' = 0$. When the intercavity coupling is smaller than the effective dissipation rate, the local minimum becomes the only peak.

From this paper, and comparing Eq. (14) with Eq. (17), one can see that the transmission peaks do not coincide with the eigenfrequencies (vertical black solid and dotted line in Fig. 3).

Figure 3 presents transmission spectra for different phases ϕ and relative coupling κ. For a phase $\phi = \pi/2$ (solid and dashed red curve), the coupling J is minimal, and the effective detuning $\Delta' = \Delta$. As shown in Fig. 2(a), the condition $J > \Gamma$ is never satisfied, independently of κ. Therefore, there is only one maximum in the transmission spectrum for this phase, located at ω_0, the cavity resonance. This maximum is equal to 1 when there are no losses ($\kappa = 1$) and decreases with decreasing κ.

When the phase $\phi < \pi/2$ (dotted and dashed-dot red curve), one transmission peak appears for a frequency smaller than ω_0 (a negative detuning Δ) due to the coupling between the two cavities. The location of the two peaks is given by the first two relations of Eq. (17). This equation is used to plot the vertical black line in Fig. 2 for $\phi = \pi/5$ and $\kappa = 1$. Once again, if $\kappa < 1$, the maximum transmission is smaller than 1 because of the dissipation inside the cavities.

For phases $\phi > \pi/2$ (blue curves) the second transmission peak appears at frequencies larger than the cavity resonance (detuning $\Delta > 0$). The horizontal dashed black line gives the maximal transmission for $\kappa = 0.9$ and $\phi = \pi/5, 4\pi/5$. Finally, the dotted horizontal black line represents the minimal transmission for $\kappa = 1$ and $\phi = \pi/5, 4\pi/5$.

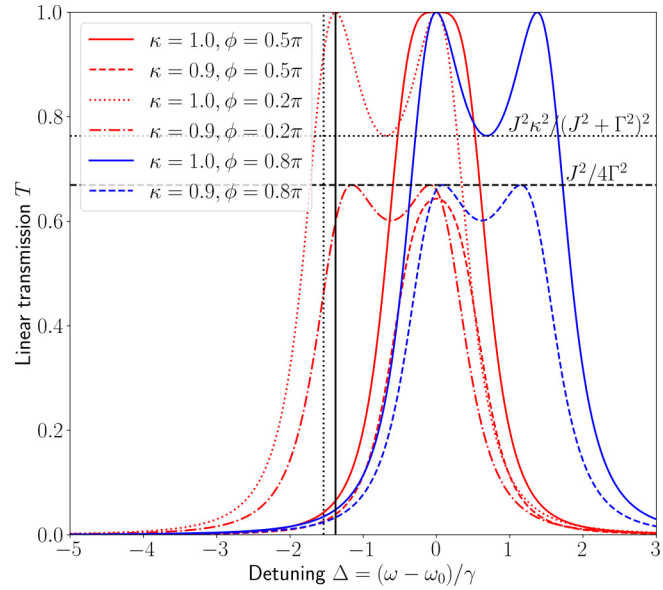

FIG. 3. Transmission (curves) in the linear regime. The vertical black line represents one frequency at maximum transmission, given by Eq. (17) for $\kappa = 1$ and $\phi = \pi/5$. The dotted black line is the eigenfrequency of the associated symmetric mode. The dashed horizontal line represents the maximum transmission for $\kappa = 0.9$, $\phi = \pi/5$ (or $\phi = 4\pi/5$). The dotted horizontal line indicated the local minimal transmission for $\kappa = 1$ and $\phi = \pi/5$ (or $\phi = 4\pi/5$).

V. NONLINEAR ANALYSIS

In order to understand the phenomena occurring at relatively high input powers, we now investigate the effects of nonlinearity. As we have performed for the linear regime, we first derive the eigenmodes of the system, then, the transmission in the nonlinear regime.

As a first step, we show that, by fixing the outgoing power, it is possible to obtain steady states analytically. Indeed, considering steady state ($\dot{\psi}_i = 0$), and by fixing the outgoing power, $|f_3^s|^2$, one can find ψ_2^s from Eq. (4). Then, using Eq. (3), ψ_1^s can be computed, leading to a corresponding pump f_1^s given by Eq. (1),

$$\psi_1^s = -\frac{1}{J}\left[\left(\Delta' + |\psi_2^s|^2\right) - j\Gamma\right]\psi_2^s, \tag{18}$$

$$f_1^s = e^{-j(\phi/2)}\left\{\left[\left(\Delta' + |\psi_1^s|^2\right) - j\Gamma\right]\psi_1^s + J\psi_2^s\right\}. \tag{19}$$

In these equations, the superscript s stands for the steady state.

A. Perturbative analysis

We are now interested in obtaining an eigenvalue problem for the nonlinear regime. As for the linear case, it will provide an understanding of the damping and frequencies of the system eigenmodes through the real and imaginary parts of the eigenvalues.

For the nonlinear eigenmodes, we consider no pumping ($f_1 = 0$) and no noise ($N_i = 0$) in Eq. (10). By linearizing Eq. (10) around the steady state and denoting the right-hand side of this equation h_i,

$$\dot{\tilde{\Psi}}_i = h_i(\tilde{\Psi}) \simeq \underbrace{h_i(\tilde{\Psi}^s)}_{0} + \left.\frac{\partial h_i}{\partial \tilde{\Psi}_k}\right|_{\tilde{\Psi}^s} \left(\tilde{\Psi}_k - \tilde{\Psi}_k^s\right), \tag{20}$$

where $\tilde{\Psi} = (\psi_1, \psi_1^*, \psi_2, \psi_2^*)^T$. In this last relation, $D_{ik} = \frac{\partial h_i}{\partial \tilde{\Psi}_k}|_{\tilde{\Psi}^s}$ is an element of the Jacobian matrix of the nonlinear system. By considering a first-order perturbation, $\psi_i(t) \simeq \psi_i^s + \delta\psi_i(t)$, one obtains the relation $\delta\dot{\tilde{\Psi}} = D\,\delta\tilde{\Psi}$ where the Jacobian,

$$D = \begin{pmatrix} -j\left(\Delta' + 2\left|\psi_1^s\right|^2\right) - \Gamma & -j\psi_1^{s^2} & -jJ & 0 \\ j\psi_1^{*s^2} & j\left(\Delta' + 2\left|\psi_1^s\right|^2\right) - \Gamma & 0 & jJ \\ -jJ & 0 & -j\left(\Delta' + 2\left|\psi_2^s\right|^2\right) - \Gamma & -j\psi_2^{s^2} \\ 0 & jJ & j\psi_2^{*s^2} & j\left(\Delta' + 2\left|\psi_2^s\right|^2\right) - \Gamma \end{pmatrix}. \tag{21}$$

In order to obtain the desired eigenvalue problem as proposed in previous literature [30,32], one writes the perturbation fields as

$$\delta\psi_i = u_i e^{\lambda\tau} + v_i^* e^{\lambda^*\tau} \tag{22}$$

leading to the secular equation (see the Supplemental Material [31]),

$$D\Psi' = \lambda\Psi', \tag{23}$$

where $\Psi' = (u_1, v_1, u_2, v_2)^T$ is the vector of fluctuation amplitudes and λ is the eigenvalue of the perturbed fields, sometimes called Bogoliubov modes [30,32]. As for the linear analysis, examining the real and imaginary parts of λ gives the eigenmode damping and frequencies for the perturbations.

In addition, the perturbative analysis provides a way to analyze the stability of the steady states. As $\delta\psi_i \sim e^{\lambda\tau}$, by observing the real and imaginary parts of the eigenvalues, we can distinguish between stable and unstable states. If the four eigenvalues have negative real parts, the mode will be damped and, therefore, stable (S). On the other hand, if one of them is positive, the steady state will be one mode unstable ($1M$) when the corresponding imaginary part is zero. Finally, if there is a pair of complex conjugates with positive damping (real part of λ) it leads to parametric instability (PU). As a result, self-pulsing can be observed where for a constant pump intensity, the outgoing power varies. Furthermore, in this situation, chaotic behavior is possible and can be predicted by numerically solving Eqs. (1)–(6) and computing the maximal Lyapunov exponent of the resulting time series. This is not reported in the current paper, so we only focus on stable parametrically unstable and one-mode unstable states.

B. Transmission

As we have performed in the linear regime, we study the nonlinear transmission spectra. With a real and positive nonlinearity α, the transmission peaks are redshifted with increasing pump amplitude. Therefore, in the noninear regime,

$$T = \frac{\kappa^2 n_2}{n_1[(\Delta' + n_1)^2 + \Gamma^2] + J^2 n_2 - 2n_2(\Delta' + n_2)(\Delta' + n_1) + 2n_2\Gamma^2}, \tag{24}$$

where $n_i = |\psi_i^s|^2$ is the stationary dimensionless energy in cavity i. As the energy n_1 is a function of the effective detuning Δ' [see Eq. (18)], the transmission extrema are given by a general polynomial of order 5. According to the Abel-Ruffini theorem, there is no closed form for the roots. However, we find that (when $\kappa \simeq 1$) a good approximation is as follows:

$$\Delta' \simeq \pm\sqrt{J^2 - \Gamma^2} - n_2, \tag{25}$$

which corresponds to the linear peaks, shifted by n_2 as represented by the green dashed lines in Fig. 4. Indeed, if internal losses are small with respect to coupling with external ports ($\kappa \simeq 1$) when the transmission is maximal, the energy inside cavity 2 (n_2) must be high. As the redshift of the cavity resonances is directly proportional to n_i in Eq. (10), a similar shift appears in the transmission peaks.

As the transmission is now a function of the frequency and the pump intensity, we consider transmission maps in Fig. 4. Because in particular regimes, multiple steady states exist for one incoming power, we consider the transmitted power $|f_3|^2$ instead of the incoming power $|f_1|^2$ in these maps. Indeed, Eqs. (18) and (19) give a direct link between the transmitted field and the fields in the cavities.

Using the previously derived stability analysis, we can determine the various stability regions. Three situations are shown in Fig. 4 corresponding to the same relative coupling $\kappa = 1$ (no internal losses) but different phases ϕ. When $\phi = \pi/5$ [Fig. 4(a)], just like the linear regime, there are two transmission peaks at frequencies given by Eq. (25) and represented by the green dashed lines. PU, corresponding to self-pulsing, arise when the cavity energy $n_2 = |\psi_2|^2$ overcomes the losses $\Gamma = 0.5$ [30], and for frequencies lying between the transmission peaks. When $\phi = \pi/2$ [Fig. 4(b)],

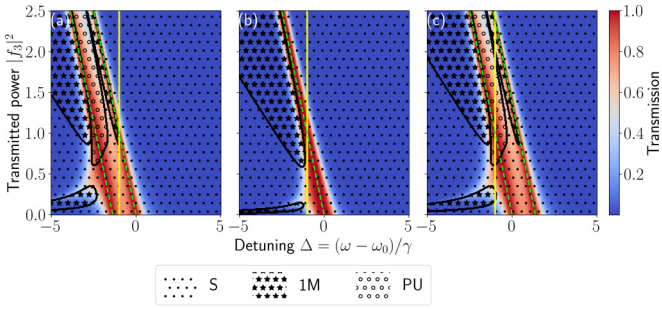

FIG. 4. Transmission and steady-state stability versus detuning and outgoing power for $\kappa = 1$ and (a) $\phi = \pi/5$, (b) $\phi = \pi/2$, and (c) $\phi = 4\pi/5$. S are dotted regions, PU are circle regions, and one-mode unstable ($1M$) states are star regions. The vertical yellow line represents the detuning $\Delta = -1$ used in Figs. 7 and 8. The dashed green lines are given by Eq. (25) and correspond to transmission maxima.

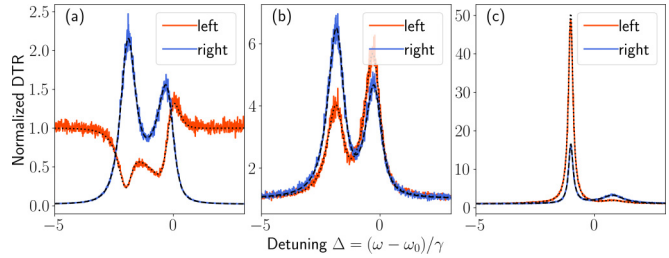

FIG. 5. DTR normalized by maximum thermal energy ($k_B T$) where T is the largest temperature in the system. Numerical simulations (noisy red and blue curves) are compared to analytical solutions (black dashed and dotted lines) for (a) $\kappa = 1$, $|f_1|^2 = 0.625$, $\Delta = -1$, $T_{e_L} = 500$, $T_{e_C} = T_{e_R} = 10$ K and $\phi = \pi/2$. (b) $\kappa = 0.9$, $|f_1|^2 = 0.670$, and $\Delta = -1$, all the temperatures at 300 K and $\phi = \pi/2$. (c) $\kappa = 0.9$, $|f_1|^2 = 0.540$, and $\Delta = -1$, all the temperatures at 300 K and $\phi = 4\pi/5$.

the coupling J is minimal. Therefore, there is only one maximum for the transmission (green dashed line), and in this situation there are no PU states. Finally, for a phase $\phi = 4\pi/5$ [Fig. 4(c)], the coupling is the same as for $\phi = \pi/5$, but the effective detuning is different. Thus, the transmission peaks start, for low power, at the resonance of the cavity and at a larger frequency. Then, due to the nonlinearity, both peaks are redshifted. In the three graphs, the vertical yellow line corresponds to the detuning value Δ used in the next section. There are also regions where the system is $1M$ meaning that the fixed point corresponding to the couple (detuning, output power) is unstable. It arises when the system supports multistability i.e., multiple stable states for the same input power, which is discussed in the Supplemental Material [31].

VI. THERMAL RADIATION

Now that we have derived analytical equations for the steady state and eigenmodes in both the linear and the nonlinear regimes, we focus on the derivation of thermal radiation. It turns out that, when the steady state is stable, it is possible to derive a useful analytical solution for the outgoing thermal radiation to the left and right channels.

The cavity field amplitudes as well as the forward and backward waveguide fields undergo fluctuations due to the temperature, which are described via random processes. These fluctuations are defined as deviations from the average value. For example, the fluctuations of the left output field are $\delta b_1(t) = b_1(t) - \langle b_1(t)\rangle$, where $\langle\cdot\rangle$ means "ensemble averaging."

As in previous literature, we define the density of thermal radiation (DTR) as the spectral density of fluctuations, which we note as $\langle|\delta b_1(\omega)|^2\rangle$ for the left waveguide and $\langle|\delta f_3(\omega)|^2\rangle$ for the right one. It is computed as the difference between the total power spectral density $\langle|f_3(\omega)|^2\rangle$ and the coherent power spectral density $|\langle f_3(\omega)\rangle|^2$. Indeed, as all noise sources have zero average, $\langle f_3(\omega)\rangle$ corresponds to the coherent outgoing field.

To obtain an analytical solution for the left and right output DTR, which characterizes thermal emission from the system, we follow these steps. First, we decompose $\psi_i(t)$ as $\psi_i^s + \delta\psi_i(t)$ and separate the evolution of the coherent part and the fluctuations (see the Supplemental Material [31]). Second, we Fourier transform the resulting equations for the fluctuations to obtain four equations in the frequency domain. Finally, we combine these equations and after some calculus we obtain (see the Supplemental Material [31]) the desired functions,

$$\langle|\delta b_1(\omega)|^2\rangle = \langle|\xi_{e_L}(\omega)|^2\rangle + \kappa^2\langle|\delta\psi_1(\omega)|^2\rangle + 2\kappa\,\mathrm{Re}[je^{-j\phi/2}\langle\delta\psi_1(\omega)\xi^*_{e_L}(\omega)\rangle], \quad (26)$$

$$\langle|\delta f_3(\omega)|^2\rangle = \langle|\xi_{e_R}(\omega)|^2\rangle + \kappa^2\langle|\delta\psi_2(\omega)|^2\rangle + 2\kappa\,\mathrm{Re}[je^{-j\phi/2}\langle\delta\psi_2(\omega)\xi^*_{e_R}(\omega)\rangle]. \quad (27)$$

The full analytical expressions of Eqs. (26) and (27) can be found in the Supplemental Material [31]. In both equations, the first term expresses the DTR from the temperature in the corresponding channel (left/right), the second is proportional to the emissivity of the cavity coupled into this channel. Interestingly, the third term represents interference between the cavity-emitted and waveguide-reflected radiation. DTR does not only take into account the emissivity of the cavities. The pump leads to an active system with another source of emitted radiation that strongly interferes with and modulates the passive behavior. As a result, even when normalized by the thermal energy from the highest system temperature, the DTR can be larger than 1.

The validity of this analytical model is checked by comparing it with numerical simulations (Fig. 5). Numerical solutions of Eqs. (1)–(6) are obtained by using a stochastic Runge-Kutta homemade solver with averaging over 500 simulations. By inspecting Fig. 5, it is clear that there is an excellent agreement among Eqs. (26), (27), and the simulations, independent of the relative coupling κ, phase ϕ, or the temperature combination. As the analytical solutions accurately predict the DTR, in what follows, we use the equations instead of simulations.

A. Linear regime

With the analytical form, first we study the low pumping regime, when the nonlinearity can be neglected. One expects to observe peaks in the thermal radiation at

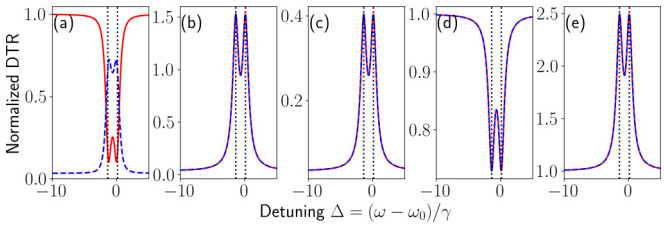

FIG. 6. Reduced DTR in the linear regime ($|f_1|^2 = 10^{-3}$) for left (solid red) and right (dashed blue) waveguides with $\phi = \pi/5$, $\kappa = 0.9$, and $\Delta = -1$. (a) $T_{e_L} = 300$ K, and the others equal 10 K. (b) $T_{e_C} = 300$ K, and the others equal 10 K. (c) $T_{d_1} = T_{d_2} = 300$ K, and the others equal 10 K. (d) $T_{e_L} = T_{e_R} = 300$ K, and the others equal 10 K. (e) All equal 300 K. Dotted vertical lines represent eigenfrequencies [Eq. (14)].

eigenfrequencies given by Eq. (14), which as noted are different from the transmission maxima [Eq. (17)]. As the system is driven asymmetrically, both symmetric and antisymmetric eigenmodes are excited, and we expect to observe peaks in the DTR for both modes.

From the linear analysis (Sec. IV) there are two eigenmodes, so one expects two DTR peaks. As an example, we consider input power $|f_1|^2 = 10^{-3}$, phase $\phi = \pi/5$, relative coupling $\kappa = 0.9$, and detuning $\Delta = -1$ (represented by the yellow vertical line in Fig. 4). We now explore various combinations for the temperatures of the waveguides and cavities, leading to qualitatively different spectra.

When the temperature of the left channel is larger than the others [Fig. 6(a)], the left thermal radiation (red line) presents two dips at the two eigenfrequencies (dotted black lines). These dips arise because as the left temperature dominates, there is destructive interference between the reflected and the emitted radiation by the first cavity [last term in Eq. (26)]. The DTR is normalized to the highest thermal energy in the system ($k_B T$). Therefore, far from the eigenfrequencies (peaks and dips), the DTR is 1 for the left channel (red plain line) and $T_{e_R}/T_{e_L} \simeq 0.033$ for the right one (blue dashed line). Indeed, far from the eigenfrequencies, the influence of the cavities is negligible, and the DTR is instead fully determined by the ratio between the temperature of the considered port and the maximum system temperature.

When the temperature of the central connecting waveguide dominates [Fig. 6(b)], the left and right DTRs are equal as the system is symmetric regarding the temperatures. When the temperatures of the cavities dominate [Fig. 6(c)], the spectra are symmetric as well for the same reason. The maximum DTR is smaller than in the previous case because there is thermal radiation toward the central waveguide as well.

When both external waveguides have a high temperature [Fig. 6(d)], both left and right spectra present two eigenmode dips due to destructive interferences on both sides. Finally, when all temperatures are equal [Fig. 6(e)], the spectra are similar to Figs. 6(b) and 6(c). The system is symmetric, and the left and right channels do not dominate, leading to no DTR dips. The maximum DTR in Fig. 6(e) is larger than in Fig. 6(b) because the whole system is at 300 K and contributes to the thermal radiation. As all the temperatures are the same, the DTR is 1 for frequencies far from the eigenmodes.

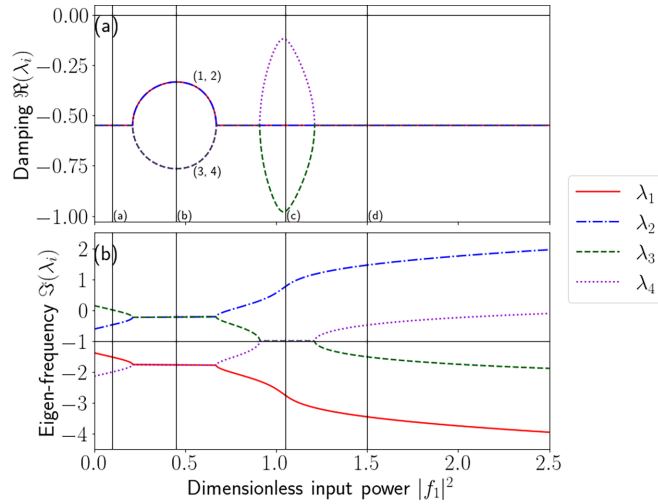

FIG. 7. Eigenvalues of the Jacobian Eq. (21) for $\kappa = 0.9$, $\Delta = -1$, and $\phi = \pi/5$. Each color/line style represents a different mode. (a) Damping of the mode. (b) Frequency of the mode relative to the pump detuning Δ. Vertical black lines and letters correspond to pump amplitudes used in Figs. 9 and 11.

B. Nonlinear regime

As mentioned in the perturbative analysis, there are four perturbed (Bogoliubov) modes. Just like in the linear regime, we expect that the frequencies of these modes correspond to the peaks and dips of the DTR spectra. Furthermore, by analyzing the real and imaginary parts of the eigenvalues, we can discuss the stability of the steady states and their influence on the DTR spectra. Figures 7 and 8 show the evolution of the four eigenvalues versus incoming power from the left $|f_1|^2$ for two different phases ϕ.

One first notes [Figs. 7(b)] and 8(b) that the imaginary parts are symmetric around the detuning $\Delta = -1$, meaning that the perturbed eigenmode frequencies are symmetric around the

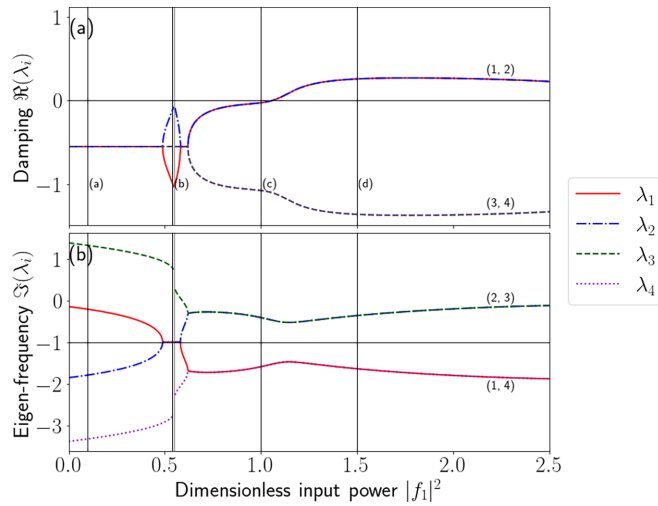

FIG. 8. Eigenvalues of the Jacobian Eq. (21) for $\kappa = 0.9$, $\Delta = -1$, and $\phi = 4\pi/5$. Each color/line style represents a different mode. (a) Damping of the mode. (b) Frequency of the mode relative to the pump detuning Δ. Vertical black lines and letters correspond to pump amplitudes used in Fig. 10.

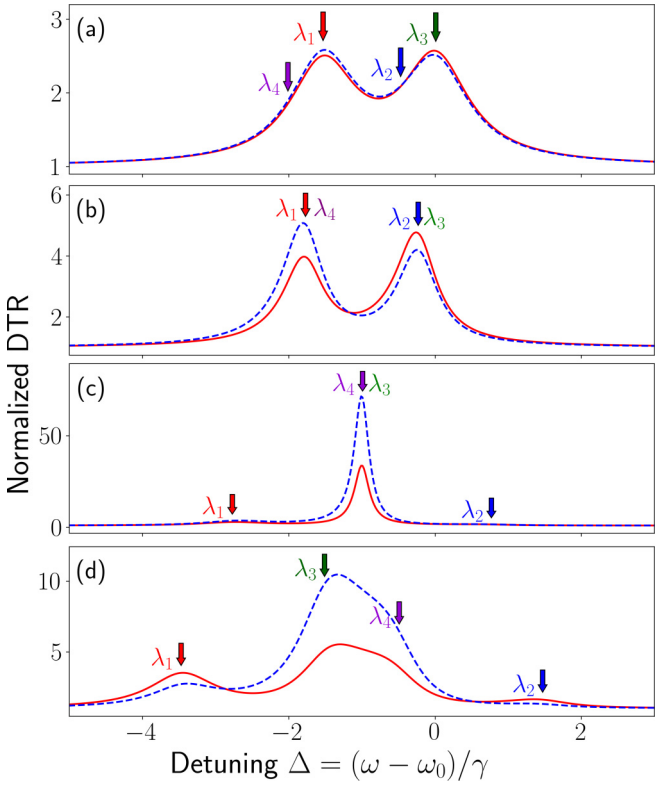

FIG. 9. Density of thermal radiation versus detuning when all temperatures are equal to 300 K for $\kappa = 0.9$, $\Delta = -1$, and $\phi = \pi/5$. (a) $|f_1|^2 = 0.1$, (b) $|f_1|^2 = 0.45$, (c) $|f_1|^2 = 1.05$, and (d) $|f_1|^2 = 1.5$. The red solid and blue dashed curves correspond to left and right ports, respectively. Arrows indicate the location of Bogoliubov modes.

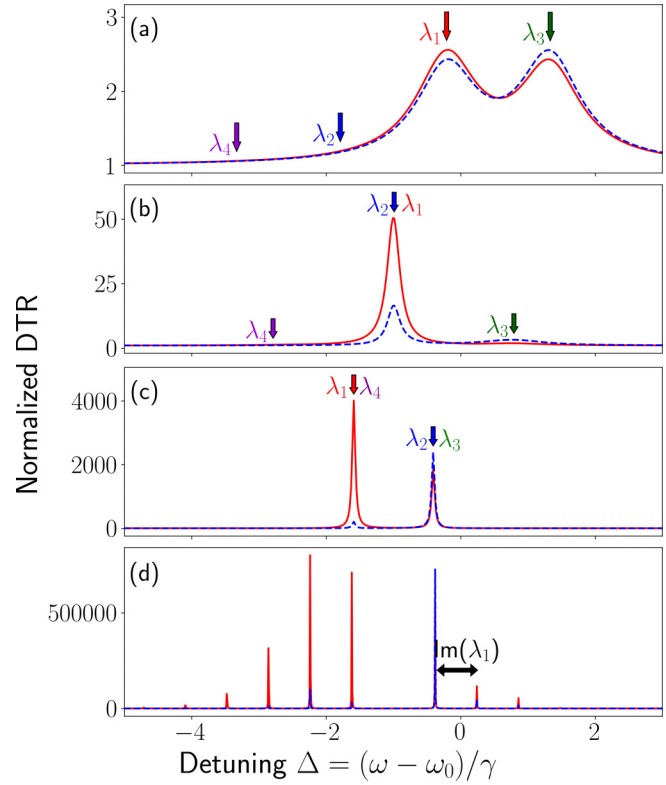

FIG. 10. Density of thermal radiation versus detuning when all temperatures are equal to 300 K for $\kappa = 0.9$, $\Delta = -1$, and $\phi = 4\pi/5$. (a) $|f_1|^2 = 0.1$, (b) $|f_1|^2 = 0.54$, (c) $|f_1|^2 = 1.0$, and (d) $|f_1|^2 = 1.5$. The red solid and blue dashed curves correspond to left and right ports, respectively. Arrows indicate the location of Bogoliubov modes.

pump. The modes corresponding to λ_1 and λ_3 (Figs. 7 and 8) are redshifted due to the chosen nonlinearity ($\alpha > 0$). The two other modes, mirrored with respect to the pump (λ_2 and λ_4) are, therefore, blueshifted when the pump intensity increases.

Second, either one or both redshifted eigenfrequencies can cross the pump (cross the horizontal black line corresponding to the detuning $\Delta = -1$) depending on phase ϕ. Indeed, in the linear regime (small $|f_1|^2$), one redshifted mode [Im(λ_1)] is smaller than the pump frequency $\Delta = -1$ for $\phi = \pi/5$ [Fig. 7(b)] whereas both of them [Im($\lambda_{1,3}$)] are larger than the detuning when $\phi = 4\pi/5$ [Fig. 8(b)].

In order to relate Figs. 7 and 8 to the spectra of Figs. 9 and 10, one should understand that by damping, we mean the real part of the eigenvalue (λ_i). Therefore, when the damping becomes positive, the corresponding mode becomes unstable or parametrically unstable. So in this context, the more negative the damping, the more damped the mode.

For the thermal properties, we first consider all temperatures equal, a phase $\phi = \pi/5$ and a relative coupling $\kappa = 0.9$. Close to the linear regime, for $|f_1|^2 = 0.1$ (first vertical line in Fig. 7), mode 3 has a larger frequency than the pump whereas mode 1 has a smaller one. As the pump power is relatively small, only two peaks, corresponding to quasilinear modes, are visible in the density of thermal radiation [Fig. 9(a)].

For increasing pump intensity, $|f_1|^2 = 0.45$, nonlinear effects start to be visible and the redshifted eigenfrequencies cross the blueshifted ones [Fig. 7(b)]. The damping rates (real parts) of the corresponding modes vary drastically [Fig. 7(a)]: Two of the modes become more damped (more negative real part), whereas the others follow the opposite trend. As a result, the modes corresponding to $\lambda_{1,2}$ are amplified, and the DTR presents two peaks centered around the pump [Fig. 9(b)] with larger amplitudes than in Fig. 9(a).

Continuing to increase the incoming power, $|f_1|^2 = 1.05$, the redshifted mode λ_3 becomes resonant with the pump. As the blueshifted modes are symmetric around the pump, λ_4 crosses the pump as well. Therefore, both modes share the same frequency and the resonance with the pump leads to a large amplification of the associated peak. Consequently, the DTR at this power [Fig. 9(c)] presents a large peak at the pump frequency, reaching more than $50k_BT$ for the right port, as well as two smaller peaks, symmetric around the pump for modes 1 and 2. These two peaks are much smaller than the one corresponding to λ_4 because these modes are not resonant with the pump and are, therefore, more damped than λ_4.

Finally, for an even larger pump power ($|f_1|^2 = 1.5$, rightmost vertical line in Fig. 7), the eigenfrequencies continue to red or blueshift. Therefore, the DTR exhibits [Fig. 7(d)] four peaks that move farther apart as the incoming power continues to increase. Each of these peaks corresponds to one of the Bogoliubov modes.

To summarize, the two linear modes (1 and 3) lead to two DTR peaks for small input power. Then, due to the

nonlinear frequency redshifting, these peaks move toward smaller frequencies until mode 3 becomes resonant with the pump leading to a large amplification of the corresponding peak. Finally, after crossing the pump, all four modes become visible in the DTR. It happens because both redshifted modes are beyond the pump frequency and blueshifted modes are always mirrored around the pump. Therefore, one can expect four peaks only after both redshifted modes have crossed the pump frequency.

In what we have just analyzed (for a phase $\phi = \pi/5$ and a detuning $\Delta = -1$), all the steady states are stable, independently of the input power [vertical yellow line in Fig. 4(a)]. When we consider $\phi = 4\pi/5$ (with the same detuning), Fig. 4(c) indicates instead regions with parametric instability or one-mode instability with consequences for the DTR.

When $\phi = 4\pi/5$ (Fig. 8), close to the linear regime ($|f_1|^2 = 0.1$), the redshifting eigenmode frequencies (1 and 3) are both larger than the pump [Fig. 8(b)]. This is because the effective detuning Δ' is smaller than Δ (negative detuning deviation in Fig. 2(b). The corresponding DTR presents two peaks located close to the linear modes [Fig. 10(a)].

For larger pump intensity, when $|f_1|^2 = 0.54$, modes 1 and 2 cross the pump and become resonant with it. The DTR, therefore, presents a large peak at the pump frequency [Fig. 10(b)]. Just beyond this point, there is a narrow region (gray vertical line in Fig. 8) where the system is one-mode unstable, which means there are multiple steady states corresponding to one input power. Our analytical solution does not work in such a situation because the noise in the system can induce jumps between the steady state. Therefore, an analytical solution should describe the transition probabilities between these states to be able to accurately predict the DTR spectra.

For an incoming power $|f_1|^2 = 1.0$, the redshifted mode 1 and blueshifted mode 4 merge (same imaginary part but different real parts). Right after the imaginary parts of these modes merge, the corresponding damping rates vary strongly with the input power. As the modes are symmetric around the pump, the same arises for modes 2 and 3. The damping rates of modes 1 and 2 are close to zero, meaning that the system is close to a PU region. This region appears in the stability map in Fig. 4(c). As the damping is very small, the DTR presents very large and narrow peaks at the eigenfrequencies [Fig. 10(c)], reaching around $4000 k_B T$ for the left port. These two peaks are symmetric around the pump.

Finally, when the pump amplitude is even larger, for example $|f_1|^2 = 1.5$, the system enters the PU region and starts a self-pulsing regime. For a steady input power, the cavity energies oscillate periodically in time. The analytical solution for the DTR does not capture this kind of regime, therefore, numerical computations must be performed to obtain the spectra. We see [Fig. 10(d)] that the DTR is a comb with the main peaks corresponding to modes 1 and 2, and higher-order modes spaced by one eigenfrequency. Indeed, as the left and right DTR depend on the cavity energies, if these energies vary periodically, this is translated into a comb in the DTR. The frequency separating the peaks corresponds to the pulsation frequency [$\mathrm{Im}(\lambda_1)$] of this regime.

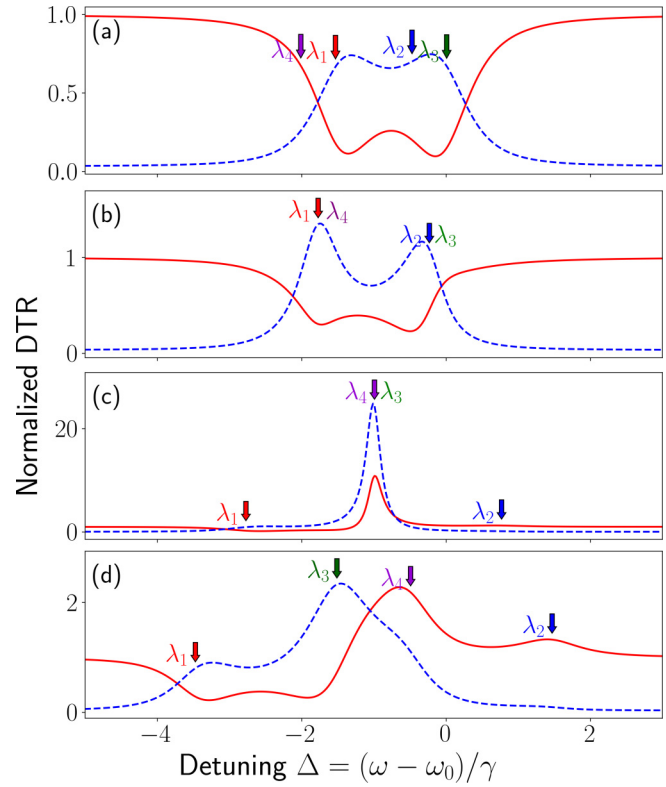

FIG. 11. Density of thermal radiation versus detuning when all temperatures are equal to 10 K except $T_{e_L} = 300$ K for $\kappa = 0.9$, $\Delta = -1$, and $\phi = \pi/5$. (a) $|f_1|^2 = 0.1$, (b) $|f_1|^2 = 0.45$, (c) $|f_1|^2 = 1.05$, and (d) $|f_1|^2 = 1.5$. The red and blue curves correspond to left and right ports, respectively. Arrows indicate the location of Bogoliubov modes.

C. Varying the temperatures

In the previous Section, we examined nonlinear emission spectra when all the temperatures are equal. However, parts of the system could be cooled or heated independently, and we noted this affects the spectra in the linear regime (Sec. VI A). Indeed, the transmitted and reflected radiation by the cavities can interfere and lead to minima in the DTR.

As an example, we show the DTR when the temperature of the left port is 300 K, whereas the rest of the system is cooled to 10 K, see Fig. 11 (other parameters the same as in Fig. 9). Destructive interference takes place in the left port, leading to dips for linear modes 1 and 3 at low power [red curve, Fig. 11(a)] as well as for modes 1 and 2 for higher power, when $|f_1|^2 = 0.45$ [red curve, Fig. 11(b)]. As the temperature of the right port is not higher than the rest of the system, there are no such dips for the DTR corresponding to the right port [blue curves, Figs. 11(a) and 11(b)]. When a mode becomes resonant with the pump, the contribution of destructive interference does not dominate, and the DTR still presents one larger peak at the pump [Fig. 11(c)]. However, the amplitude of this peak is reduced compared to the previous case where all temperatures are equal [Fig. 9(c)]. Finally, for $|f_1|^2 = 1.5$ [Fig. 11(d)], the destructive interference only dominates for the redshifted modes (λ_1, λ_3). The blueshifted ones (λ_2, λ_4) still lead to peaks in the DTR, but their amplitudes are smaller than when all temperatures are set to 300 K.

VII. CONCLUSION

We study a system of coupled nonlinear photonic cavities where the coupling arises only via the central waveguide, so an effective coupling and detuning can be derived. With this analysis, we predict the frequency of symmetric and antisymmetric modes in the linear regime. We demonstrate that the location of the eigenfrequencies differs from the frequencies of maximum transmission. We present the conditions to observe two peaks of maximum transmission by comparing the coupling and the effective damping rate.

Using a perturbative analysis, we derive the eigenfrequency and damping of the perturbed nonlinear modes. With a stability analysis, one can distinguish stable, one-mode unstable, and parametrically unstable regions, based on the system parameters. We show that parametrically unstable states do not appear if the phase is equal to $\pi/2$ when the effective coupling is minimum. We also derive a semianalytical solution for the transmission peak location in the nonlinear regime.

Based on the perturbative analysis, we explore thermal radiation from this system. We distinguish the thermal radiation from the left and right ports. In the linear regime, we show that the peaks in thermal radiation correspond to eigenmodes and not to the transmission peaks. With asymmetric pumping, both symmetric and antisymmetric modes are excited. When the temperatures of the left and/or right ports are larger than the rest of the system, destructive interference between emitted and reflected radiation by the cavity leads to dips in the DTR. Nonlinear absorption could be added to the model. This effect was explored for a single-cavity situation [14], leading to broader peaks but not yet for coupled systems. The system could be implemented, for example, using a silicon platform consisting of ring resonators coupled to a waveguide, driven at milliwatt powers as derived for a single cavity [15]. Thermo-optic nonlinearities in this platform could be subdued by working at lower temperatures, e.g., below 100 K, which does not change the reported spectral shapes as displayed in the Supplemental Material [31].

We derive an analytical solution for the description of the DTR under the stable steady-state assumption. This model presents an excellent agreement with numerical simulations based on coupled mode theory and the Langevin framework. Using this model and by analyzing the perturbed modes, we present a rich variation of thermal emission spectra. When a mode becomes resonant with the pump, it leads to supernarrow thermal radiation around the pump. Moreover, close to parametrically unstable regions, the system exhibits supernarrow peaks for the two redshifted modes, symmetric around the pump. In the self-pulsing regime, the DTR adopts a comb shape with peaks spaced by the frequency of perturbed modes.

Finally, we explore the role of temperatures on the DTR. As in the linear regime, changing the relative temperatures modifies the shape of the emission spectra. In particular, when the left or right ports have larger temperatures, destructive interference can lead to dips in the DTR. However, in a regime with supernarrow peaks, the contribution of these interferences does not dominate, and the amplitude of the peaks is just slightly smaller. In the end, the large variety of observed spectra offers interesting opportunities for fully tailorable thermal radiation via coupled nonlinear photonic resonators.

ACKNOWLEDGMENTS

This work was supported by the Fonds pour la Formation à la Recherche dans l'Industrie et dans l'Agriculture (FRIA) and by the Fonds National de Recherche Scientifique (FNRS) in Belgium. Computational resources have been provided by the Consortium des Équipements de Calcul Intensif (CÉCI), funded by the Fonds de la Recherche Scientifique de Belgique (F.R.S.-FNRS) under Grant No. 2.5020.11 and by the Walloon Region.

APPENDIX A: ROTATING FRAME

In order to obtain Eqs. (1)–(4), we proceed to a rotating frame at the pump frequency ω_p. Let a_i be the field amplitude in the cavity i with normalization such that $|a_i|^2$ represents the energy in the cavity. Moreover, let f_i' and b_i' be the forward (backward) fields in a waveguide such that $|f_i'|^2$ ($|b_i'|^2$) represents the power going forward (backward) in the waveguide. In such a situation, the temporal coupled mode equations describing the system are as follows:

$$\frac{da_1}{dt} = [j(\omega_0 - \alpha|a_1|^2) - \gamma]a_1 + je^{j(\phi/2)}\sqrt{\gamma_e}\left(f_1' + \xi_{e_L}'\right) + je^{j(\phi/2)}\sqrt{\gamma_e}\left(b_2' + \xi_{e_C}'\right) + \sqrt{2\gamma_d}\xi_{d_1}' \tag{A1}$$

$$b_1' = e^{j\phi}\left(f_1' + \xi_{e_L}'\right) + j\sqrt{\gamma_e}e^{j(\phi/2)}a_1 \tag{A2}$$

$$\frac{da_2}{dt} = [j(\omega_0 - \alpha|a_2|^2) - \gamma]a_2 + je^{j(\phi/2)}\sqrt{\gamma_e}\left(f_2' + \xi_{e_{C'}}'\right) + je^{j(\phi/2)}\sqrt{\gamma_e}\left(b_3' + \xi_{e_R}'\right) + \sqrt{2\gamma_d}\xi_{d_2}' \tag{A3}$$

$$f_3' = e^{j\phi}\xi_{e_R}' + j\sqrt{\gamma_e}e^{j(\phi/2)}a_2. \tag{A4}$$

In these equations, the noise sources are real with variance $\Theta(\omega, T_k)$ where $k \in \{e_L, e_C, e_C', e_R, d_1, d_2\}$. As the pump is monochromatic, $f_1'(t) = f_1'e^{j\omega_p t}$ meaning that all the fields will oscillate at ω_p. Taking $\psi_i(t) = \sqrt{\alpha/\gamma}a_i(t)e^{-j\omega_p t}$, $f_i(t) = \sqrt{\alpha\gamma_e/\gamma^3}f_i'(t)$, and the same for backward fields, one obtains with $\tau = \gamma t$, Eqs. (1)–(4).

Now, due to the rotating frame, the noise sources are complex with uncorrelated real and imaginary parts due to the fast oscillation of $\langle \mathrm{Re}(\xi_k)\mathrm{Im}(\xi_k)\rangle$ [28]. The noise sources follow the correlation relations given in Eqs. (7) and (8).

APPENDIX B: ORIGINAL FREQUENCY AND DISSIPATION RATE

As the eigenvalues λ_k satisfy

$$\frac{d\psi_i}{d\tau} = \lambda_k\psi_i, \quad k \in \{+,-\} \quad \text{and} \quad i \in \{1,2\}, \tag{B1}$$

and because $\psi_i(t) = \sqrt{\alpha/\gamma}a_i(t)e^{-j\omega_p t}$, one can show that

$$\frac{da_i}{d\tau} = \gamma(\lambda_k + j\omega_p)a_i \tag{B2}$$

resulting in Eqs. (14) and (15).

APPENDIX C: FIELDS IN THE CENTRAL WAVEGUIDE

In the central waveguide we consider two reference planes 2 and 2′, see Fig. 1. The backward and forward fields are

related via

$$f_2 = e^{j\phi} b_2 + j\kappa e^{j(\phi/2)} \psi_1 \tag{C1}$$

$$b_{2'} = e^{j\phi} f_{2'} + j\kappa e^{j(\phi/2)} \psi_2 \tag{C2}$$

$$f_{2'} = e^{j\theta} f_2 \tag{C3}$$

$$b_2 = e^{-j\theta} b_{2'} \tag{C4}$$

where θ is a phase term that depends on the distance between the planes. With the correct central waveguide length, so plane choice, θ can be a multiple of 2π resulting in $e^{j\theta} = e^{-j\theta} = 1$ and $b_2 = b_{2'}$, $f_2 = f_{2'}$. Therefore, one obtains

$$f_2 = e^{j\phi} b_2 + j\kappa e^{j(\phi/2)} \psi_1, \tag{C5}$$

$$b_2 = e^{j\phi} f_2 + j\kappa e^{j(\phi/2)} \psi_2, \tag{C6}$$

which can be combined to give Eqs. (5) and (6).

[1] S. Basu, Y.-B. Chen, and Z. M. Zhang, Int. J. Energy Res. **31**, 689 (2007).

[2] S. Wijewardane and D. Y. Goswami, Renewable Sustainable Energy Rev. **16**, 1863 (2012).

[3] S. Fan, Nat. Nanotechnol. **9**, 92 (2014).

[4] S. Kawata, Y. Inouye, and P. Verma, Nat. Photonics **3**, 388 (2009).

[5] A. Lenert, D. M. Bierman, Y. Nam, W. R. Chan, I. Celanović, M. Soljačić, and E. N. Wang, Nat. Nanotechnol. **9**, 126 (2014).

[6] A. Kittel, W. Müller-Hirsch, J. Parisi, S.-A. Biehs, D. Reddig, and M. Holthaus, Phys. Rev. Lett. **95**, 224301 (2005).

[7] Y. De Wilde, F. Formanek, R. Carminati, B. Gralak, P.-A. Lemoine, K. Joulain, J.-P. Mulet, Y. Chen, and J.-J. Greffet, Nature (London) **444**, 740 (2006).

[8] A. Kittel, U. F. Wischnath, J. Welker, O. Huth, F. Rüting, and S.-A. Biehs, Appl. Phys. Lett. **93**, 193109 (2008).

[9] F. Huth, M. Schnell, J. Wittborn, N. Ocelic, and R. Hillenbrand, Nature Mater. **10**, 352 (2011).

[10] S. M. Rytov, Y. A. Kravtsov, and V. I. Tatarskii, *Principles of Statistical Radiophysics 2: Correlation Theory of Random Processes* (Springer, Berlin, 1988).

[11] D. Polder and M. Van Hove, Phys. Rev. B **4**, 3303 (1971).

[12] W. Eckhardt, Phys. Rev. A **29**, 1991 (1984).

[13] O. Ilic, M. Jablan, J. D. Joannopoulos, I. Celanovic, and M. Soljačić, Opt. Express **20**, A366 (2012).

[14] C. Khandekar, A. Pick, S. G. Johnson, and A. W. Rodriguez, Phys. Rev. B **91**, 115406 (2015).

[15] C. Khandekar, Z. Lin, and A. W. Rodriguez, Appl. Phys. Lett. **106**, 151109 (2015).

[16] S. Buddhiraju, W. Li, and S. Fan, Phys. Rev. Lett. **124**, 077402 (2020).

[17] B. Braeckeveldt and B. Maes, J. Opt. Soc. Am. B **39**, 2074 (2022).

[18] J. Testa, J. Pérez, and C. Jeffries, Phys. Rev. Lett. **48**, 714 (1982).

[19] R. Lifshitz and M. C. Cross, Phys. Rev. B **67**, 134302 (2003).

[20] C. Stambaugh and H. B. Chan, Phys. Rev. B **73**, 172302 (2006).

[21] S. Malaguti, G. Bellanca, A. de Rossi, S. Combrié, and S. Trillo, Phys. Rev. A **83**, 051802(R) (2011).

[22] J. Yelo-Sarrión, P. Parra-Rivas, N. Englebert, C. M. Arabí, F. Leo, and S.-P. Gorza, Phys. Rev. Res. **3**, L042031 (2021).

[23] N. Carlon Zambon, S. R. K. Rodriguez, A. Lemaître, A. Harouri, L. Le Gratiet, I. Sagnes, P. St-Jean, S. Ravets, A. Amo, and J. Bloch, Phys. Rev. A **102**, 023526 (2020).

[24] J. Yelo-Sarrión, F. Leo, S.-P. Gorza, and P. Parra-Rivas, Phys. Rev. A **106**, 013512 (2022).

[25] K. J. H. Peters, Z. Geng, K. Malmir, J. M. Smith, and S. R. K. Rodriguez, Phys. Rev. Lett. **126**, 213901 (2021).

[26] B. Maes, P. Bienstman, and R. Baets, J. Opt. Soc. Am. B **22**, 1778 (2005).

[27] G. Altares Menendez and B. Maes, Phys. Rev. B **100**, 014306 (2019).

[28] M. I. Dykman, D. G. Luchinsky, R. Mannella, P. V. E. McClintock, N. D. Stein, and N. G. Stocks, Phys. Rev. E **49**, 1198 (1994).

[29] B. Garbin, A. Giraldo, K. J. H. Peters, N. G. R. Broderick, A. Spakman, F. Raineri, A. Levenson, S. R. K. Rodriguez, B. Krauskopf, and A. M. Yacomotti, Phys. Rev. Lett. **128**, 053901 (2022).

[30] D. Sarchi, I. Carusotto, M. Wouters, and V. Savona, Phys. Rev. B **77**, 125324 (2008).

[31] See Supplemental Material at http://link.aps.org/supplemental/10.1103/PhysRevB.107.174310 for the calculation of the transmission function; the derivation of the eigenvalue problem for perturbed modes; an example of the transmission function in the multistable regime; the relation between thermal radiation and the power spectral density; the full derivation of the analytical formula for thermal radiation.

[32] C. Ciuti and I. Carusotto, Phys. Status Solidi B **242**, 2224 (2005).